energies

MDPI

Article

Influence of Water Saturation on the Mechanical Behaviour of Low-Permeability Reservoir Rocks

Decheng Zhang, Ranjith Pathegama Gamage *, Mandadige Samintha Anne Perera, Chengpeng Zhang and Wanniarachchillage Ayal Maneth Wanniarachchi

Deep Earth Energy Laboratory, Department of Civil Engineering, Monash University, Building 60, Melbourne 3800, Australia; decheng.zhang@monash.edu (D.Z.); samintha.perera@unimelb.edu.au (M.S.A.P.); chengpeng.zhang@monash.edu (C.Z.); ayal.maneth@monash.edu (W.A.M.W.)

* Correspondence: ranjith.pg@monash.edu; Tel.: +61-3-9905-4982

Academic Editor: Moran Wang

Received: 5 October 2016; Accepted: 9 January 2017; Published: 16 February 2017

Abstract: The influence of water on the mechanical properties of rocks has been observed by many researchers in rock engineering and laboratory tests, especially for sedimentary rocks. In order to investigate the effect of water saturation on the mechanical properties of low-permeability rocks, uniaxial compression tests were conducted on siltstone with different water contents. The effects of water on the strength, elastic moduli, crack initiation and damage thresholds were observed for different water saturation levels. It was found that 10% water saturation level caused more than half of the reductions in mechanical properties. A new approach is proposed to analyze the stress-strain relations at different stages of compression by dividing the axial and lateral stress-strain curves into five equal stress zones, where stress zones 1–5 refer to 0%–20%, 20%–40%, 40%–60%, 60%–80% and 80%–100% of the peak stress, respectively. Stress zone 2 represents the elastic range better than stress zone 3 which is at half of the peak stress. The normalized crack initiation and crack damage stress thresholds obtained from the stress-strain curves and acoustic emission activities averaged 31.5% and 83% of the peak strength respectively. Pore pressure is inferred to take part in the deformation of low-permeability siltstone samples, especially at full saturation levels. A change of failure pattern from multi-fracturing to single shear failure with the increase of water saturation level was also observed.

Keywords: water degradation; water saturation level; low-permeability; uniaxial compressive strength (UCS); mechanical properties

1. Introduction

The mechanical properties of rocks in the upper crust are important in underground and geotechnical engineering projects, including tunnelling, drilling and reservoir exploration. However, rocks' physical and mechanical properties are influenced by the type of pore fluid [1] and the saturation level [2,3]. Water is the most common saturation medium and can be present in rocks at any level. The existence of water can be classified into five types: structural water as a component of minerals like clay; bounded water on the surfaces of minerals, especially hydrophilic minerals like montmorillonite, due to electrochemical reactions; water physically trapped by capillaries; water in small pores with limited mobilization and free water in large pores and fractures. Furthermore, the water saturation level may change due to geological changes or human intervention, like earthquakes, excavation, injection or extraction of fluids from underground reservoirs. With the depletion of conventional oil reservoirs over their life cycles, water is used to enhance oil production by replacing the oil in place, which causes changes in the saturation medium and saturation level. In addition, hydraulic fracturing is widely used to stimulate unconventional oil and gas reservoirs by introducing water into

the target formations and extracting water during production. Therefore, significant changes in the water saturation levels of reservoirs during the fracturing and production processes are inevitable. As a result, precise evaluation of the effect of water saturation on the variation of mechanical properties of host rocks is important for oil and gas exploration design, especially in low-permeability rocks.

The effect of water on rock mechanical properties has been studied for many types of rocks [4], and Wong et al. [3] found that sedimentary rocks are more sensitive to water than igneous and metamorphic rocks. Obvious reductions in uniaxial compressive strength (UCS) [5] and Young's modulus have been shown with the introduction of water to sandstone [6], clay [7], mudrock [2] and coal [8]. The degradation of mechanical properties is a function of the water content, where exponential or power relations are usually shown [3,9]. According to previous studies, moisture reduction in rocks can result in increases in their stiffness and strength [10,11], especially for rocks with high clay contents. Although, degradations in elastic moduli are generally assumed with increases in moisture content, it has been reported that the Young's modulus of wet samples at the initial compression stage can be higher than those of dry samples because of the more pronounced pore and crack shrinkage of the dry samples [12].

There are many definitions of Young modules and Poisson's ratio in the rock mechanics field and various methods have been introduced to evaluate them [13,14]. The values obtained from different approaches may be different. For example, secant Young's modulus is lower than that obtained from the linear part of the stress-strain curve and the Poisson's ratio calculated using the American Society for Testing and Materials (ASTM)-recommended method is larger than that derived from the crack closure to the crack initiation stress threshold range [15]. According to Vásárhelyi [16], there is an almost constant ratio of 0.82 for the E_{secant} / $E_{tangent}$ based on the data on 35 sandstones. Therefore, it is necessary to compare values obtained by different approaches and find the appropriate methods to evaluate the elastic moduli.

The studying of crack propagation also assists in identifying the mechanical characteristics of rocks, particularly the brittleness characteristics. Eberhardt et al. [15] proposed that the stress-strain curves are characterized by the crack closure, crack initiation and damage stress thresholds and demonstrated methods to obtain these thresholds. Amann et al. [17] showed that the crack initiation threshold was about 0.3 of the UCS and the crack initiation process was accompanied by the onset of inelastic strain and acoustic emission, while the crack damage threshold characterized the volume deformation transition from the compaction to dilation [18]. Studies show that water diffusing to the tips of the fractures can lower the thresholds for crack propagation for rocks, ceramics and single crystals of quartz [18]. Others also demonstrate that water can reduce the crack initiation and crack damage thresholds [19,20]. In addition to the stress-strain curves, acoustic emission (AE) during loading can also be used to identify the stress thresholds characteristics [15]. However, AE signal intensity for wet samples are much lower than those for dry samples due to the softening effect of water in the rock mass weakening the fracturing process [21,22]. The deformations or failure patterns also vary with water saturation [6]. The weakening effects of water on rocks are generally attributed to the chemical reactions between water and minerals, especially the clay-water reactions [7], pore pressure [17], reduction of friction between grains [23], the surface energy [12] and the test conditions. However, most of the experiments have been conducted on high-permeability rocks like sandstones, or only consider the totally dry and full saturation levels. Therefore, detailed descriptions of the effect of different water saturation levels on low-permeability rock mechanical properties including strength, elastic modulus, crack initiation and damage thresholds and failure patterns are needed.

The understanding and prediction of water-weakening effects on rock mechanical properties are vital in rock engineering designs in terms of rock failure. In order to test the water weakening effects on low-permeability rocks with different water saturation levels, a series of UCS tests was conducted using siltstone.

2. Experiments

2.1. Sample Description and Preparation

The samples in our tests were Eidsvold siltstone from Queensland, Australia, formed during the Mesozoic era, and the siltstone blocks were provided by a local quarry. The blocks were cored into cylinders 38 mm in diameter in the Monash University Civil Engineering Department Laboratory, and were then cut and ground to 76 mm in length with parallel and smooth end faces for the UCS tests according to the ASTM standard [14]. As the siltstone samples used are relatively homogeneous, the coring direction had little effect on the mechanical properties and there was little deviation in the test results. X-ray diffraction (XRD) tests were conducted on the siltstone powders using an Empyrean diffractometer (Panalytical, Almelo, The Netherlands) with a step size of 0.02° for a step duration of 1 s, and a combination of matrix flushing and reference intensity ratio (RIR) derived constants was used in the quantification of the minerals. Scanning electron microscope (SEM) images were obtained for the thin slices of the siltstone samples using a 7001F field emission SEM machine (JEOL, Tokyo, Japan) located at the Monash Centre for Electron Microscopy (MCEM). The basic properties and the mineral composition based on XRD testing of the Eidsvold siltstone are shown in Table 1. According to the XRD results, quartz and kaolinite are the most abundant minerals in the siltstone which is confirmed by Figure 1, while there is little swelling clay minerals. The mercury intrusion porosimetry (MIP) test was conducted with a small bulk dry siltstone sample. The sample was evacuated under 50 μmHg for 5 min, and the mercury filling pressure was 0.52 psia. The range of the mercury filling pressure was 0.1–60,000 psia and the equilibration time was 10 s for both the low- and high-pressure filling. The contact angle between the mercury and the siltstone used to calculate the pore size was 130°.

Table 1. Properties of dry Eidsvold siltstone. MIP: mercury intrusion porosimetry.

Density	Porosity	Vp	Vs	Alpha Quartz	Kaolinite	Tridymite	Mica	Anatase	Other Clay Mineral
g/cm^3	MIP	km/s	km/s	Percentage by weight					
2.220	19.45%	4.04	2.59	43%	40%	12%	3%	1%	<1%

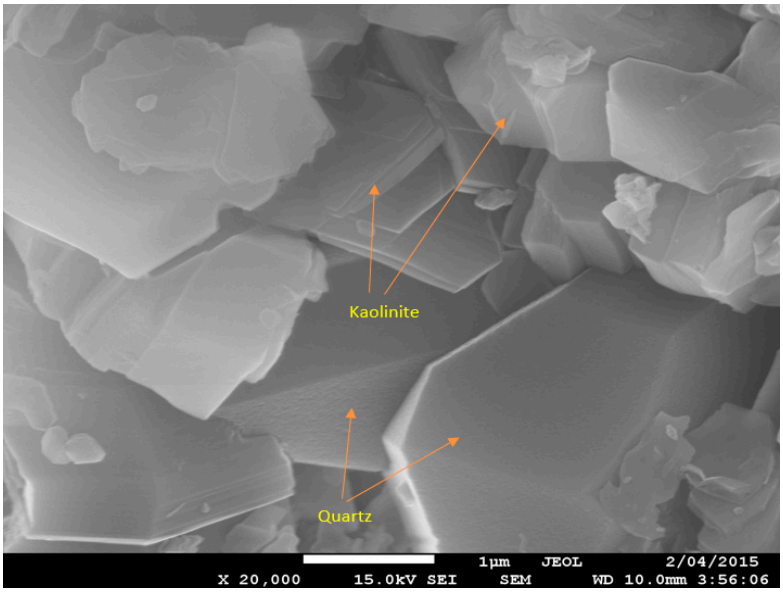

Figure 1. Scanning electron microscope (SEM) image showing the microstructure and minerals of the siltstone sample.

Figure 2 shows the incremental intrusion volume vs. pore size in the mercury intrusion test, and the larger pore size at the first peak was caused by the destruction during the sample preparation

process and the pore diameter ranges from several nanometers to several micrometers [24], which is confirmed by the SEM images in Figure 3. Although the siltstone was fine-grained, a high porosity up to 19.45% was obtained from the mercury intrusion tests.

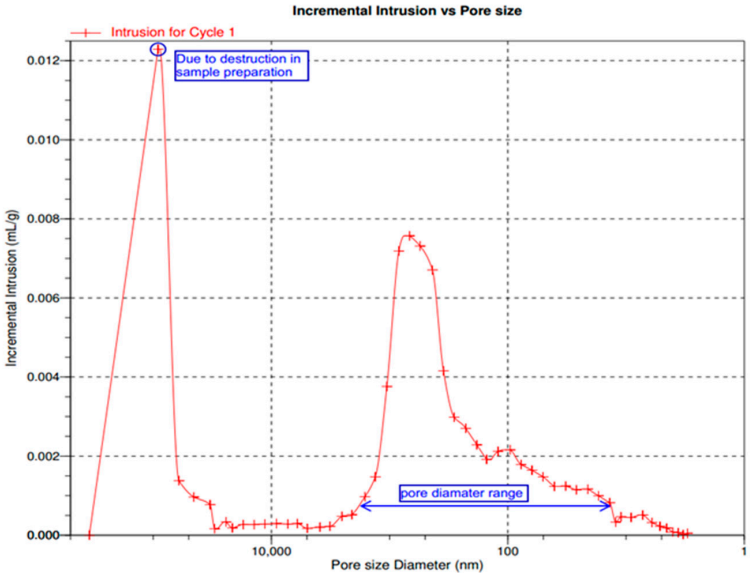

Figure 2. Incremental intrusion vs. pore size in the mercury intrusion test.

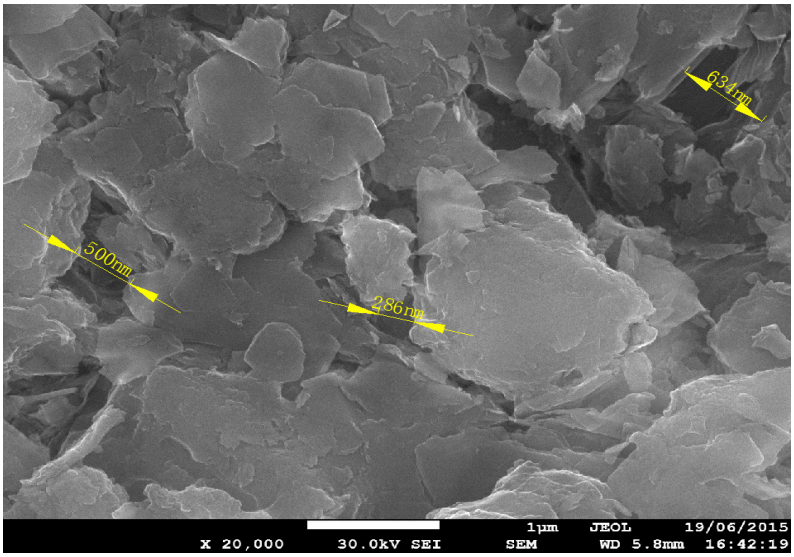

Figure 3. SEM image showing pore shape and size of the siltstone sample.

To test the influence of water content on the mechanical properties, samples were first dried for 72 h in the oven at 60 °C and then weighed. The oven temperature of 60 °C was chosen to avoid the occurrence of thermal cracking and baking of the clay minerals resulting from high temperature. Some extra samples were further dried at 100 °C for a sufficient time, and showed no further weight loss. Therefore, 60 °C for 72 h was found to be appropriate for the complete drying of the low-porosity siltstone samples. The dry samples were then saturated with de-ionized water in a vacuum chamber. Five saturation conditions were selected: 0%, 10%, 30%, 60% and 100%, with the 100% saturation level defined as immersing samples in the chamber for 30 days under vacuum conditions, and the other saturation conditions were achieved according to the weight.

It was observed that there was no mineral dissolution in the de-ionized water by comparing the initial dry weight and the dry weight after immersion in de-ionized water for more than 35 days. Therefore, the weight differences between the wet and the dry samples accurately showed the amount of absorbed water. The samples with different water saturation levels were then wrapped with several layers of cling wrap and placed in a controlled temperature and humidity environment for a month to ensure the water in the samples was evenly distributed before the tests. All the samples were then checked to see if there were any major defects or fractures upon saturation, and samples with large fractures were discarded so that only micro-cracks existed in the tested samples.

2.2. Experiment Facilities

The UCS tests were conducted using a Shimadzu AG 9 instrument (Shimadzu, Kyoto, Japan) accompanied by AE detection equipment and an optical three-dimensional (3D) deformation measuring system. The uniaxial loading was applied by the Shimadzu AG 9, which has a maximum capacity of 300 KN, and the loading rate was set at 0.1 mm/min for all the tests. The loading during the test was recorded automatically.

The non-contact optical 3-D deformation measuring system Aramis (GOM, Braunschweig, Germany) was used to record the failure process visually and to calculate the axial and lateral strains. A series of optical digital images was taken by two sensitive cameras in the Aramis system during the loading process to measure the deformation. To optically recognize the surface patterns of the almost homogeneous samples, samples were first painted white on the surface facing the cameras, then dotted with black paint to enhance the surface pattern. The Aramis system recognizes the surface structures taken by the digital cameras and allocates coordinates to the image pixels. The sample images were taken every 3 or 5 s to obtain detailed graphical images of the process. The first image was taken as the undeformed state and acted as a reference for the deformation measurements, which were calculated by the changes in coordinates in the later stages. Vertical and horizontal lines were drawn in the middle of the samples to avoid the end effect and these line strains at different stages corresponded to the axial and lateral strains respectively. By this method, the relative displacement of the loading frame and the pedestal were corrected. Figure 4 shows a painted UCS sample and the strain values calculated using the Aramis system.

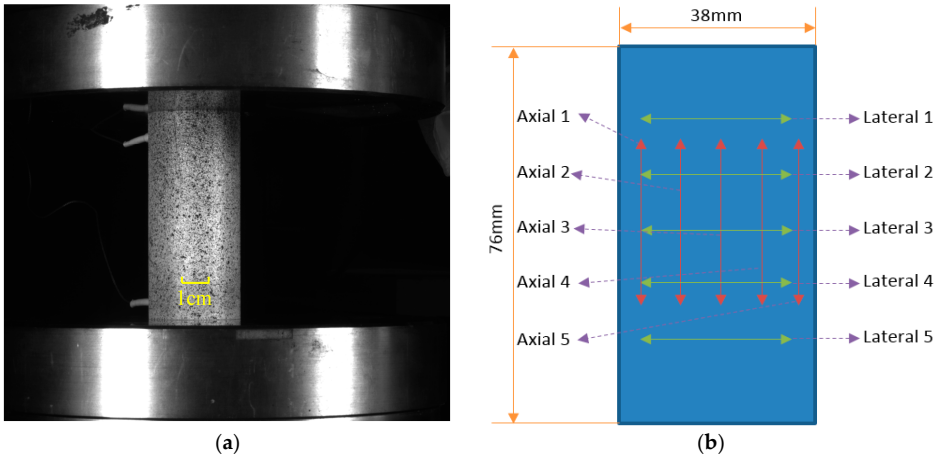

Figure 4. (**a**) Painted sample and (**b**) line strain calculations on the computed strain diagram by Aramis.

AEs are elastic waves produced by the micro-cracking of mineral grains and the cohesion between grains, sliding along the grain boundary, pore collapse and other sources. AE detection is a non-destructive physical method to monitor the energy release in stressed materials. The system used in the experiments reported here was the PCI-2 AE system manufactured by the Mistras Group Inc. (Princeton Junction, NJ, USA), which has simultaneous waveform and digital signal processing.

A preamplifier gain of 40 dB was used to increase the signal intensity and reduce the noise. Since the sample surfaces are used by the Aramis system, the two AE sensors were attached on the top and bottom platens at a distance of 20 mm to the sample surface. The AE data during the loading process were recorded over time.

2.3. Experimental Procedures

The UCS samples were first painted and then checked by the Aramis system to determine if the painted surface pattern was recognizable and good computing images could be obtained, and repainting was needed for inadequate patterns. The loading platens were then adjusted to ensure good contact with the samples before compression. The AE sensors were then attached on the top and bottom platens. The loading rate was set at 0.1 mm/min for the UCS tests to satisfy the requirement by ASTM [14] that samples failed in 5–15 min. The Shimadzu, Aramis and AE systems started simultaneously and data were logged automatically. A series of UCS experiments was conducted at different water saturation levels, and at least three samples were tested under each condition to obtain the average value.

3. Results

3.1. Uniaxial Compressive Strength with Water Saturation

UCS values were calculated based on the peak load and original sample cross-section, while the dimension change in the lateral direction of the sample during loading was ignored, since the lateral strain was small (less than 0.4%). The average UCS values and deviations at different water saturation levels are shown in Figure 5. As can be seen from the figure, the UCS values decrease with the increase of water saturation level, and a total decrease of nearly 32% is observed from dry to 100% saturation conditions. It is noteworthy that a significant reduction (18.56%) is shown with only 10% water saturation level, while little reduction occurs over 60% water saturation level.

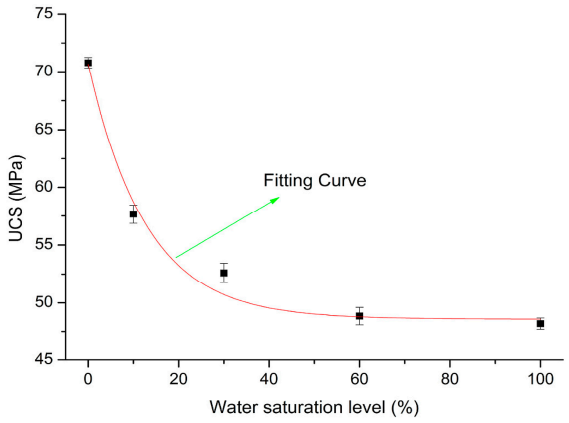

Figure 5. Calculated average uniaxial compressive strength (UCS) and deviations with water saturation level and the fitting curve.

According to Priest and Selvakumar [25], the UCS values have a negative exponential relationship to the water content:

$$\sigma_c = ae^{-bw} + c \quad (1)$$

where σ_c (MPa) is the uniaxial strength, w is the moisture content, and a, b and c are constants.

Here we replace the parameter for water content, w, with the water saturation level, s. We fitted our data with the above equation and obtained the equations below, and the fitting curve (red curve) is shown in Figure 5. The curve fits well with the experiment data, with the exception of some departure at the 30% water saturation level:

$$\sigma_c = 22.104 \times e^{-7.782s} + 48.571 \ (R^2 = 0.988) \quad (2)$$

where s is the water saturation level with s = 0 for the dry condition, and s = 1 for the fully saturated condition.

3.2. Stress-Strain Curves

The load was logged per second by the Shimadzu, then divided by the original sample cross-section area to be converted to the stress, while the strain values were calculated by the Aramis system which recorded the displacement in the axial and lateral directions every 3 or 5 s. The stress versus axial and lateral strain curves are plotted for samples with different water saturation levels in Figure 6a. The axial strain is defined as positive and lateral strain as negative by convention. Based on observation of the stress-strain curves, we can differentiate the strength and curve shape characteristics between different water saturation levels. The peak strength decreases with the water saturation, as discussed previously. Similar shapes of the stress-strain curves for samples with different water saturation levels are displayed in Figure 6a, with some differences in the slopes.

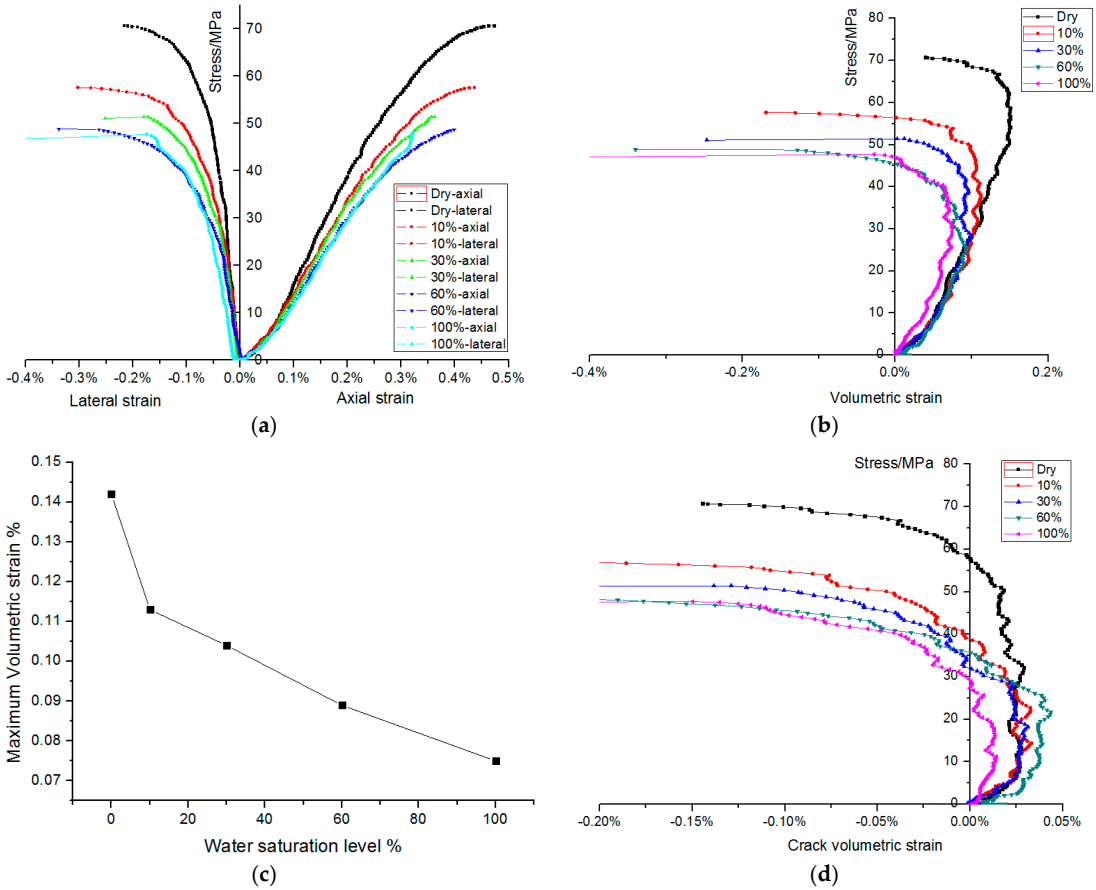

Figure 6. Calculated stress-strain curves for different water saturation levels: (**a**) stress-axial & lateral strain curve; (**b**) stress-volumetric strain curve; (**c**) maximum volumetric strain-water saturation level; and (**d**) stress-crack volumetric strain curve.

For the axial stress-strain curves, the slopes first increase, which corresponds to the closure of the pre-existing fractures aligned at an angle to the loading direction, then the slopes become almost constant, corresponding to the elastic stage, and the slopes then become smaller until the peak strength is reached, indicating the yielding and damaging process. For the lateral stress-strain curves, the curve slopes decrease with the increase of the stress and the rate of reduction of the slopes accelerates during

compression. Therefore, in the later stages before failure, the axial and lateral strain increase quickly with only limited increase in the total stress. It should be noted that the general slope decreases with the increase of the water saturation level for both the axial and lateral stress-strain curves.

The volumetric strain can be calculated using the following equation:

$$\varepsilon_v = \varepsilon_a + 2\varepsilon_l \tag{3}$$

where ε_a, ε_l and ε_v are the axial, lateral and volumetric strain respectively.

The elastic volumetric strain can be obtained by the following Equation (4):

$$\epsilon_{ev} = \frac{(1-2v) \times \sigma}{E} \tag{4}$$

where ϵ_{ev} is the elastic volumetric strain, v is the Poisson's ratio, E is the Young's modulus; and σ is the UCS.

Therefore, the crack volume strain is obtained by the difference between the volumetric strain and the elastic volumetric strain, as shown in Equation (5):

$$\epsilon_{cv} = \varepsilon_v - \epsilon_{ev} \tag{5}$$

where ϵ_{cv} is the crack volumetric strain.

The volumetric strain versus stress and maximum volumetric strain for samples under different water saturation levels are shown in Figure 6b,c respectively. The volumetric strain first increases quickly with stress as the large fractures are closed, then develops linearly, after which it becomes flat as the newly created fracture volume offsets the compressed volume. Once the newly created fractures communicate with each other and macro-cracks start to form and propagate, the volumetric strain rapidly reverses from compression to dilation. Importantly with the increasing of water saturation, the ultimate volumetric strain at failure is found to transfer from positive to negative. This indicates that increasing moisture content may cause the siltstone volumetric deformation to be transferred from compression to dilation. Figure 6c shows that the peak volumetric strain decreases with the water saturation level, as the water in the pores restricts the further compression of the pores and pre-existing fractures. There is a significant decrease in maximum volumetric strain between the dry and 10% water saturation condition due to their large strength difference, which is around 42% of total reduction from dry condition to fully saturated condition. The reduction is linear between the 10% to 100% water saturation levels with the maximum volumetric strain at fully saturated condition being 52.7% of that under the dry condition. The crack volumetric strain vs. stress is shown in Figure 6d. The figure indicates that the crack volumetric strain increases in the crack closure stage, and starts to decrease after departure from a relatively horizontal level, indicating crack initiation. The crack volumetric strain reduces significantly in the later stages, especially before failure. The crack volumetric strain decreases as the water saturation increases, possibly because more cracks are filled by water and it becomes easier for fracture initiation and propagation to occur when the water saturation level increases. It should be noted that sample deformation is also influenced by the applied strain rate, which not only affects the stiffness of the rocks under compression, but also influences the deformation characteristics, especially for wet samples with low-permeability. According to previous research, the magnitude of the volumetric strain can be significantly reduced in the elastic compression stage under high strain rates, particularly for wet samples [12] and rocks may become more brittle under higher strain rates with unevenly distributed stress and strain values [26]. Therefore, great care was taken in this study to use the same strain rates for all the load applications

According to Eberhardt et al. [15], the whole process of compression can be characterized by some thresholds showing crack closure, initiation, and damage on the stress-strain curves. The crack closure threshold can be defined by the starting point of linearity for the axial, lateral, volumetric or crack volumetric strain curves, and it is also the highest point on the crack volume strain curve. In the elastic range, the stress-strain curves will change linearly, and the crack initiation threshold can be

identified by the departure from linearity for the lateral, volumetric, or crack volumetric stress-strain curves which can be judged by the changes in the curve slope, because most of the fractures created are open in the lateral direction. The crack damage threshold is characterized by the reverse point from compression to dilation of the volumetric strain curve. These thresholds are picked out from the stress-strain curves and shown in Table 2.

Table 2. Observed crack closure, crack initiation and crack damage thresholds and the normalized ratios to the UCS from stress-strain curves and acoustic emission (AE). S-S: stress-strain curve.

Crack Thresholds	Crack Closure/S-S		Crack Initiation/S-S		Crack Initiation/AE		Crack Damage/S-S		Crack Damage/AE	
	Value/MPa	%	Value/MPa	%	Value/MPa	%	Value/MPa	%	Value/MPa	%
Dry	5.580	7.866	22.788	32.192	21.753	30.730	63.026	89.034	61.888	87.426
10%	3.412	5.916	19.116	33.159	18.017	31.275	48.645	84.380	48.595	84.294
30%	3.083	5.861	16.985	32.335	16.313	30.995	44.157	83.939	43.421	82.541
60%	2.708	5.249	16.137	31.287	15.608	30.261	41.465	80.394	41.133	79.750
100%	2.502	5.127	15.520	31.880	14.952	30.722	39.734	81.579	39.434	80.967
Average	-	5.675	-	32.135	-	30.816	-	83.299	-	82.600

3.3. Elastic Modulus

The stress-strain curves are normally used to calculate the Young's modulus and Poisson's ratio, which can usually be derived from the tangent or secant at half of the peak strength or the linear parts of the curve. The moving point regression technique is also proposed to calculate the E and v, and the relatively stable values are selected to represent these values [13,15]. Using the ASTM recommended approaches, we assume that an almost linear relation occurs at around half of the peak compressive strength, which is questioned by some researchers. Eberhardt et al. [15] suggested that the elastic modulus should be calculated in the phase between crack closure and crack initiation thresholds, as the lateral stress-strain and volumetric stiffness curves are linear in this stage, and the value calculated in this stage is higher than those from the ASTM recommended approaches. Amann et al. [17] showed that the crack initiation threshold ranges between 30% and 50% of the rupture stress, and the crack damage thresholds occur at around 70% of the rupture stress. Therefore there are basically five stages in the compression: (i) the crack closure stage; (ii) crack closure to crack initiation threshold (30%–50% of the peak stress) without any cracking; (iii) the middle range of the stress at half of peak stress, where the normal elastic moduli are obtained; (iv) from the middle range to that before the crack damage threshold; and (v) period after the crack damage threshold until failure. Therefore, we divided our curves into five equal stress zones (0%–20%, 20%–40%, 40%–60%, 60%–80% and 80%–100% of the UCS) to characterize these deformation patterns in different loading stages, which are consistent with the crack initiation and crack damage thresholds found by others and ensure that we also obtain the elastic moduli at around half of the peak stress for comparison.

Figure 7 shows the axial and lateral stiffness calculated in different stress zones for a dry sample and a fully saturated sample. It can be seen that apart from some deviations in the initial and final zones where the curves are non-linear, the linear regression fits well with these stress zones. The average elastic moduli in different stress zones for different water saturation levels are shown in Figure 8. However, there are several common methods used to obtain the elastic moduli from the stress-strain curves, such as the tangent and secant elastic moduli and values derived from the linear part [14]. To demonstrate the differences between the values obtained by different methods, we also calculated the tangent and secant elastic moduli. The tangent elastic moduli are based on the half of the peak stress, while the secant moduli are obtained by the slopes from the origin to the point at half of the peak stress. The tangent elastic moduli can be approximately represented by those from the 40%–60% stress zones.

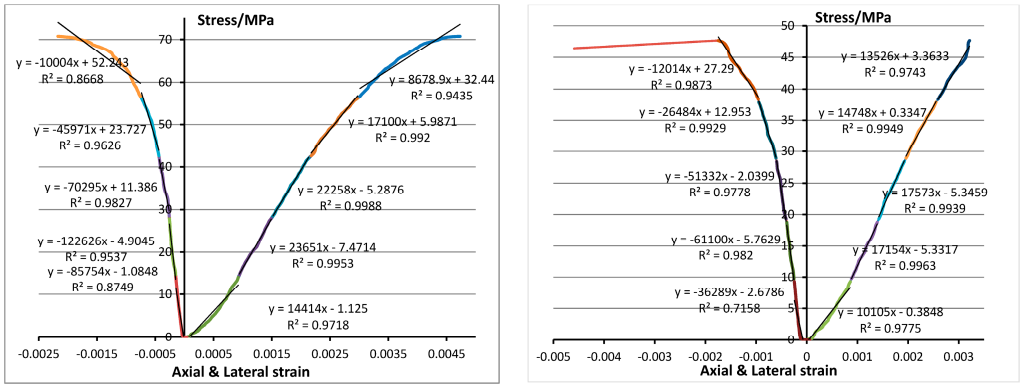

Figure 7. Axial and lateral stiffness calculated in different stress zones for (**a**) dry and (**b**) fully saturated samples.

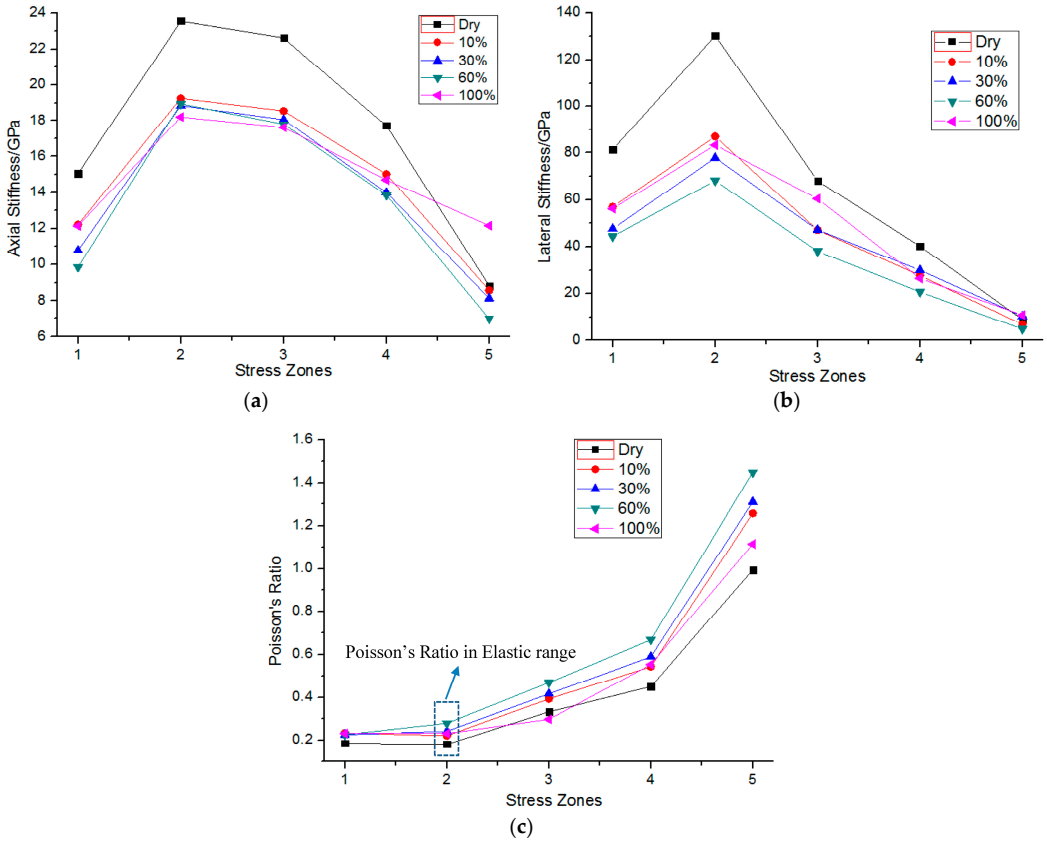

Figure 8. Elastic moduli in different stress zones and with different water saturation levels for (**a**) axial stiffness; (**b**) lateral stiffness; and (**c**) Poisson's ratio (Zones 1–5 means 0%–20%, 20%–40%, 40%–60%, 60%–80% and 80%–100% of the UCS ranges respectively).

The development of the axial stress-strain slopes discussed above is certified by the variation of the axial stiffness, which increases significantly at first, then remains stable, followed by a decreasing trend. In general, an arch shape for axial stiffness is shown for all water saturation conditions. However, the average axial stiffness between 20% and 40% of the stress range is always higher than that between 40% and 60% of the stress range, which is reasonable considering that crack initiation starts at around 30%–50% of the UCS according to Amann et al. [17]. Therefore, theoretically the stress zone between 20% and 40% represents the elastic range better than that between 40% and 60%. The axial stiffness decreases

with water saturation levels at all stress zones except at full saturation, and the largest reduction occurs between dry and 10% water saturation conditions. At full saturation, the axial stiffness is almost identical to that under 10% water saturation conditions in the first stress zone. This phenomenon can be explained by the pore water pressure. Due to capillary pressure, the water is first absorbed by the smallest pores and narrowest fractures, therefore under part-saturation conditions (10%, 30%, 60%) only the smaller pores and fractures are filled with water. However, as the main deformation in the initial loading stage comes from the large pores and fractures, no water pressure is developed in these large defects. Instead, at full saturation all the pores and fractures are water-filled, and the water is forced out of the sample when compressed. Since the pore size and the permeability of the siltstone are quite low, the water is not drained fast enough to match the speed of deformation, giving rise to pore pressure, which causes the increase in the axial stiffness. As cracking initiates in the later stages, which reduces the pore water pressure, the axial stiffness becomes lower than under other saturation conditions. Approaching failure, the micro-cracks propagate along the loading direction and open in the lateral direction, resulting in intensive lateral deformation, as the loading is axial strain-controlled, while the quick lateral deformation causes water resistance, therefore increasing the axial stiffness.

The tangent and secant Young's moduli were also calculated at half of the peak stress, and the tangent Young's modulus was close to the axial stiffness calculated at stress zone 3 (40%–60%). A comparison of the elastic Young's modulus defined at stress zone 2 (20% to 40% of the peak stress), and the tangent and secant Young's moduli at different water saturation levels are plotted in Figure 9a. The figure shows that the secant Young's modulus is the smallest, as it incorporates the initial crack closure stage, and its differences with the other two show the initial damage level [15].

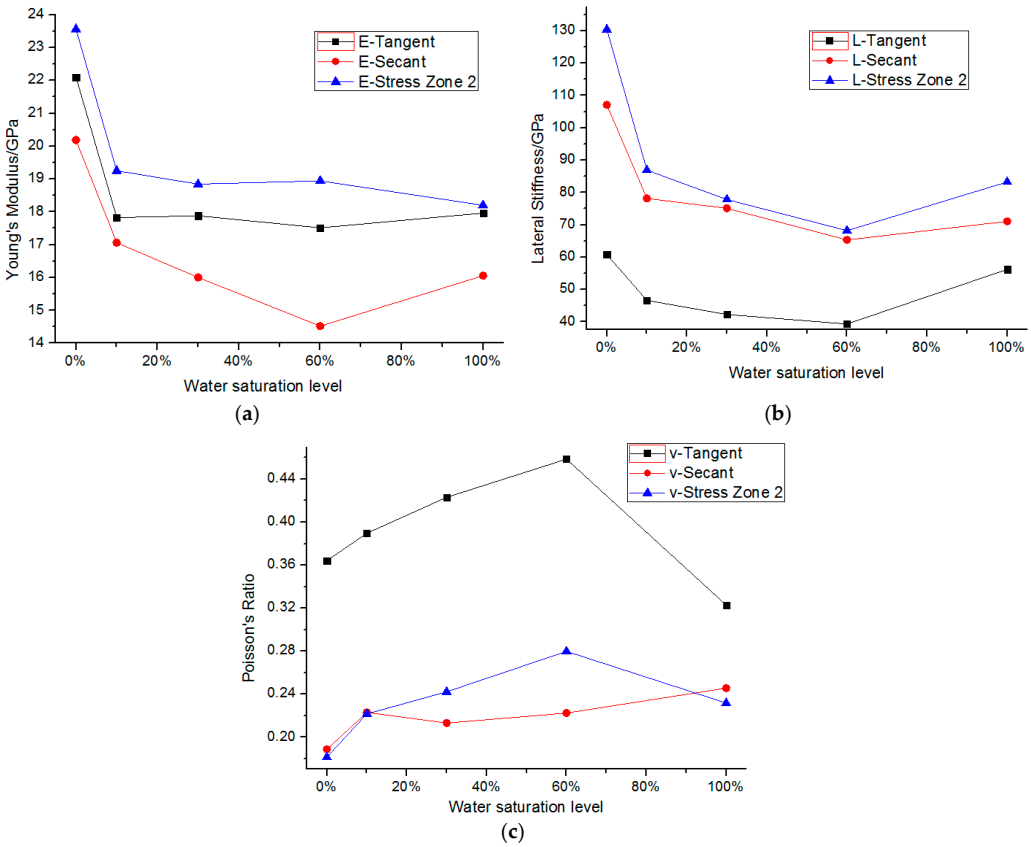

Figure 9. Comparison of tangent, secant and stress zone 2 elastic moduli for (**a**) axial stiffness; (**b**) lateral stiffness and (**c**) Poisson's ratio at different water saturation levels.

The axial stiffness at stress zone 2 is higher than the tangent Young's modulus, as explained previously. There is a significant reduction between the dry condition and the 10% water saturation level followed by a relative stable trend as the water saturation level increases further. Compared with the UCS-water saturation curve in which a continuing decreasing trend is shown, the almost stable trend with water saturation after 10% water saturation level is because the UCS is defined as the peak stress at the end of compression and no pore pressure exists as the macro-cracks form. However, the Young's modulus is calculated in the first half of the stress range and the pore pressure plays a part as the water saturation level increases.

The lateral stiffness, which is defined as the stress divided by the lateral strain, shows a similar trend to axial stiffness. At first, the deformation in the lateral direction is also large in the consolidated stage, resulting in lower lateral stiffness. It then increases at stress zone 2, followed by a reduction due to the cracks opening in the lateral direction. The values decrease with the water saturation except at full saturation. At full saturation level, the water in the pores slows the deformation, resulting in the enhancement of the lateral stiffness. In addition, the tangent and secant lateral stiffness are also calculated at half of the peak stress. The comparisons between the tangent, secant and that in the stress zone 2 are shown in Figure 9b. The tangent lateral stiffness values are always much lower than the others, as the slopes decrease with the loading process, while the lateral stiffness at stress zone 2 is a little higher than the secant values, as the secant values also incorporate the initial compression stage. The three lateral stiffness curves show the largest drops between dry and 10% water saturation level, and decrease further with the water saturation level until a gentle increase is shown at full saturation.

The Poisson's ratio can be calculated by dividing the axial stiffness by lateral stiffness, and we calculated the Poisson's ratio for different stress zones during loading with different water saturation levels. An overall increasing trend is shown for the loading process under all saturation levels with a gentle increase from stress zone 1 to 2 and a dramatic increase in the later stages especially before failure. The axial strain rate is five times the lateral strain rate in stress zone 1, while the lateral strain rate gradually becomes higher, exceeding the axial strain rate in the last stress zone. The Poisson's ratio at all stress zones increases with the water saturation level from dry to 60%, as can be seen in Figure 9c. At full saturation, the Poisson's ratio also shows an increasing trend, but it intersects with the other curves. The relatively lower Poisson's ratio values at full saturation compared with other wet samples are because initially the pore pressure prohibits axial deformation, while after crack initiation and propagation the deformation in the axial direction becomes larger. A comparison of the tangent and secant Poisson's ratios and those at stress zone 2 shows that the tangent Poisson's ratios are much higher than the others due to the lateral strain rate gradually increases with loading. For the tangent Poisson's ratio and values at stress zone 2, the Poisson's ratios first increase from dry to 60% water saturation level then decrease at full saturation, while the secant Poisson's ratio differs from the other two values by displaying an initial increase at 10% water saturation level, then becoming stable until 60% water saturation level, after which a slight increase is shown.

To better represent the elastic range of rocks during compression, zone 2 (20%–40% of peak stress) was selected since crack initiation is negligible in this stage. The crack volume strains were calculated based on the elastic moduli in stress zone 2.

3.4. Acoustic Emission Responses

As deformation is accompanied by the release of AE under compression, AE data can serve as an indicator of the response of rocks under loading. The AE activities were recorded with time and are plotted in Figure 10. In the initial stage, which corresponds to the crack closure process, the AE counts are quite small. However, once the crack initiation threshold is reached, the AE counts start to increase significantly, as much energy is dissipated in the crack-creation process. As the crack density increases, the small cracks begin to coalescence, which is more damaging to rocks and a significant amount of energy is emitted corresponding to the accelerating rate of increase of the AE count. This inflection point in the accumulative AE counts vs. stress curve in the later compression stages can been seen

as the crack damage threshold indicating crack coalescence. The stage between the crack initiation threshold and the crack damage threshold is called the stable crack propagation stage and the period from the crack damage threshold to failure is the unstable crack propagation stage. The crack initiation threshold and crack damage threshold were manually selected and marked on the AE counts vs. stress curves according to previous characteristic descriptions. These thresholds from the AE activities and those from the stress-strain curves are summarized in Table 2. It is noticeable that the total AE events decrease by almost an order of magnitude from dry to wet conditions, and the decrease has also been observed for other types of rocks [22]. The reduction in the AEs received can be accounted for in two ways. Compared with the dry samples, the reduction in thresholds for crack initiation and propagation significantly decreases the AEs generated [27], and the AEs created are more likely to decay in the transmission process in the wet samples [28].

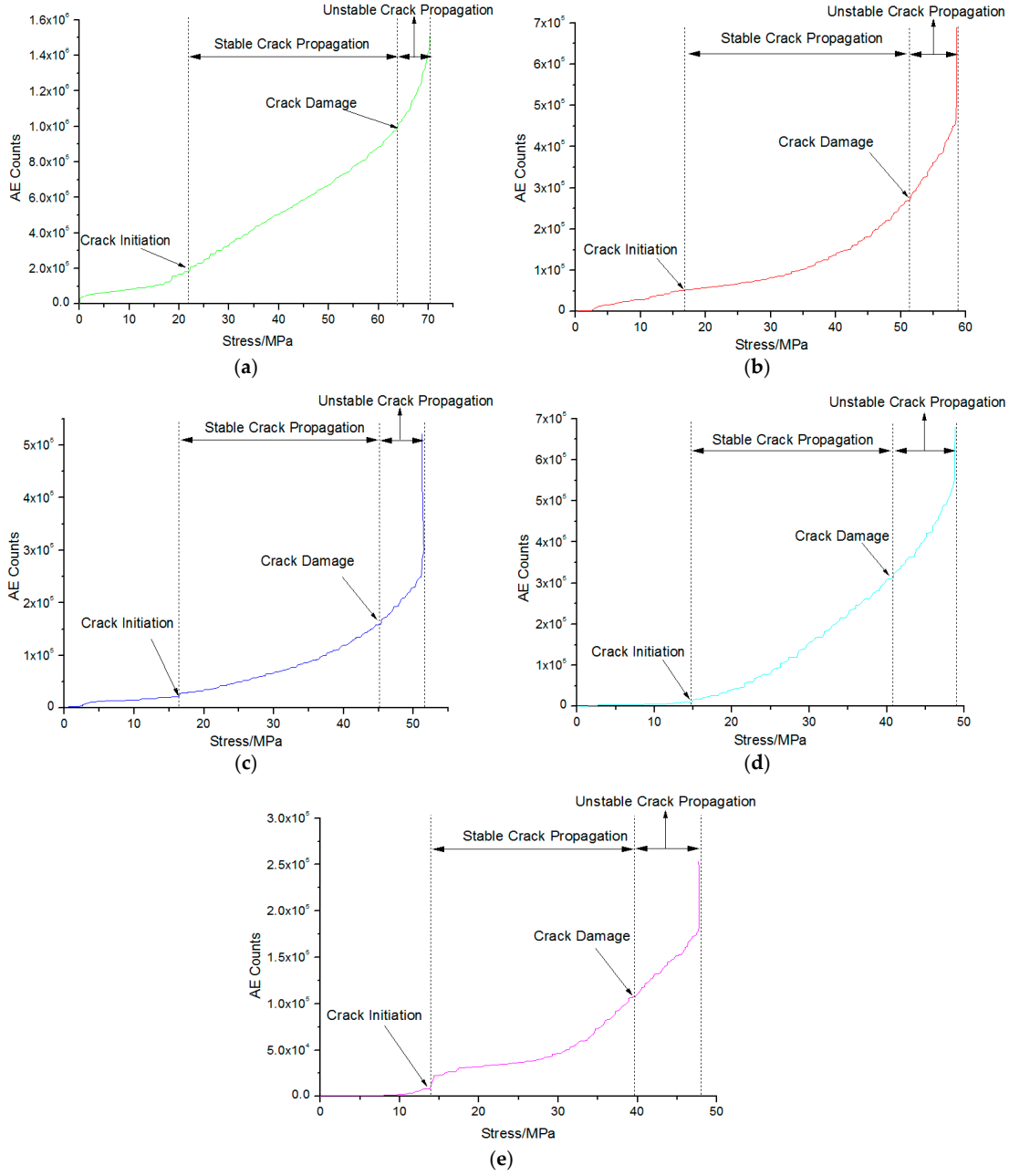

Figure 10. Accumulative AE counts vs. stress for (**a**) dry; (**b**) 10%; (**c**) 30%; (**d**) 60% and (**e**) 100% water saturation levels and their stress thresholds for crack initiation and crack damage.

As can be seen from Table 2, the thresholds for crack closure, initiation and damage derived from the stress-strain curves and the AE responses all decrease with the water saturation level, and the largest gap occurs between the dry and 10% water saturation level. When these values are normalized by the peak strength under each condition, the average ratios can be obtained by eliminating the highest and lowest values and averaging the three middle ratios. The crack closure threshold appears to be around 5.675% of the peak strength, and the ratios for the crack initiation thresholds derived from stress-strain curves and AE responses are 32.135% and 30.660%, respectively, while they are 83.299% and 82.600% for the crack damage thresholds determined from the stress-strain curve and AE performance, respectively. The normalized percentages for crack initiation and crack damage are consistent with other researchers' findings [15,17]. There are no large differences between the thresholds obtained from the stress-strain curves and AE responses, except that the values obtained from the AE activities are always slightly lower than those from the stress-strain curves. This phenomenon can be explained by the actual deformation being somewhat later than the release of the AE, which means that before any tiny shear or extremely small crack opening occurs, the release of AE already starts to increase significantly. In general, while an obvious decreasing trend is shown for the stress thresholds with the increase of water saturation level, the normalized ratios also demonstrate a gentle declining trend with water content, especially for the crack closure and crack damage ratios between the dry and 10% water saturation levels. These reductions in the normalized ratios for crack closure with water saturation levels are due to the water in the sample preventing the pores and fractures from further closing, which shortens the stage of crack closure. In addition, the declines in the normalized crack initiation and crack damage ratios show the ease of cracking and crack propagation with increased water content. Furthermore, the lower normalized ratios for the crack damage of wet samples mean that the plastic deformation is more significant for the wet samples and the yielding and failure processes for the dry samples are fast and more violent.

3.5. Failure Pattern

Due to the effects of water on the rock mechanical properties, the failure pattern is also influenced by the water content. A transformation of UCS failure pattern from axial cleavage to shear failure is found with the increase of water content [6]. Szwedzicki [29] demonstrated that UCS is a function of failure pattern and the failure patterns can be classified as axial splitting, multiple extension, multiple fracturing, multiple shear, and simple shear. Of these, axial splitting was common for intact samples with the highest UCS strength values, while single shear was common for weak samples with the lowest UCS values. Since the UCS varies with the water saturation level, changes in failure patterns are also reasonable. The optical 3-D deformation measuring system Aramis was used to record sample deformation with loading. The failure patterns and the strain diagrams computed by the Aramis system under different water saturation conditions are shown in Figure 11.

The figure shows that the calculated strain distribution diagrams well reflect the final failure pattern, and the failure pattern gradually transforms from multiple fracturing to single shear failure with the increase of water saturation level. The fracture patterns are more complex when samples are under low water saturation levels, while single shear failure dominates when samples are fully water-saturated, which is in agreement with the findings of other researchers [6,29]. As the normalized crack damage threshold ratio becomes lower as water saturation increases, the relative duration for major crack propagation increases. Therefore, the cracks probably choose one preferred path with the lowest resistance to propagation instead of branching. In addition, since the amount of energy released during unstable crack propagation becomes less for wet samples, fragmentation will not be significant and the released energy can only cause the formation of one major crack.

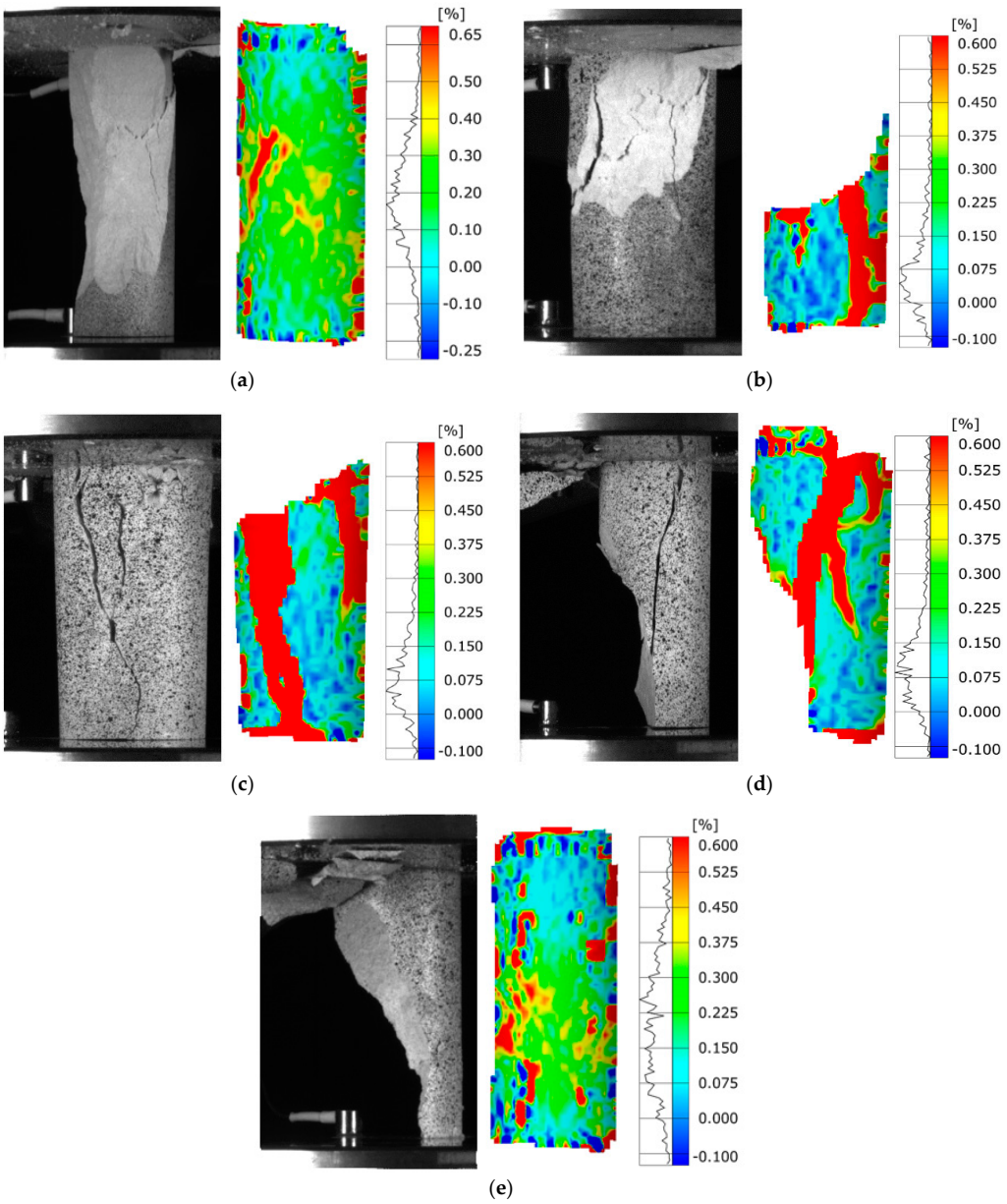

Figure 11. Failure patterns of actual siltstone samples (38 mm × 76 mm) (**left**) and the computed strain distributions at failure (**right**) by Aramis with different water saturation levels (**a**) dry; (**b**) 10%; (**c**) 30%; (**d**) 60%; and (**e**) 100%.

4. Discussion

The drastic change in the mechanical properties with low water content can be explained by the distribution of water in the samples. When water enters the sample, it is first absorbed into the smallest pores which can be several nanometers due to the capillaries [30] and onto the mineral surfaces depending on the hydrophilia. Because large numbers of small pores exist in clays and the cement minerals and both are highly hydrophilic, the water is first dispersed onto their surfaces, as the clay minerals and the cementing materials are most reactive with water by absorbing, ion exchange, and swelling [12]. Therefore, the softening is quite marked. On the other hand, the water on the surface of the minerals can significantly reduce the surface energy [12] and the frictional resistance between grains [31]. As a result, strong degradations can occur even for a small water content. With the further increase of the water saturation level, the water is stored in the large pores with limited contact with the

minerals and thus the degradation effects suffers. The siltstone used in the study is mainly constituted of quartz and kaolinite, and it has been shown that the effect of mineral dissolution and precipitation can be ignored. Although kaolinite is a non-swelling clay mineral, the high abundance and large specific surface area due to the fine grain size make the reactions drastic. Therefore, a substantial amount of degradation is induced by the water saturation. In addition, the water in the pores and fractures can keep them open if the pore fluids are not drained, which makes fracture propagation easier compared with dry closed pores and fractures. It is suggested that the water saturation condition should be precisely described in terms of mechanical testing, especially the dry state, for which a 19% increase of UCS for sandstone samples from the air-dried condition to the oven-dried condition has been reported [32].

We propose that the entire compression process can be divided into five equal stress zones in order to analyze the variation of the elastic moduli at different stages of compression. Although the stress-strain curves are not linear for the initial and last stress zones of the compression, linear regression was still applied for simplicity. Compared with one single value in the elastic range, the elastic moduli at different stress zones better describe the stress-strain relations corresponding to each stage. The tangent and secant elastic moduli and those at stress zone 2 were compared, and it was found that the elastic moduli at stress zone 2 better represent the samples' Young's modulus and Poisson's ratio for the elastic range. The normalized stress threshold for crack initiation is around 31.5%, which is located near the middle of stress zone 2. Since the small cracks are just initiated and the consolidation continues as the stress increases, the stress zone between 20% and 40% of the total stress range is appropriate for representing the elastic range, while the Young's modulus and lateral stiffness are a little lower and the Poisson's ratio is higher at stress zone 3, indicating non-negligible crack opening in the lateral direction in stress zone 3. As the average crack damage thresholds are around 83%, stress zone 5 can well represent the unstable crack propagation stage. It appears that the division into five equal stress zones is an appropriate method to characterize the elastic moduli for different stages. It should be pointed out that the elastic moduli for different water saturation levels were obtained at different stress ranges, as the UCS changes with the water content.

The samples in the tests were fine-grained and of low-permeability, and when the water saturated samples were compressed at a certain strain rate, pore pressure built up during the compression. This resulted in the relatively higher axial and later stiffness in stress zones 1 and 5 at full saturation, as the deformation was rather large in these stress zones compared with the others. The pore pressure varied during the crack closure, crack initiation and damage processes. Since the UCS values were derived at the ultimate peak strength point where the macro-cracks were formed while the elastic moduli were generally obtained at stress zones 2 and 3 where the pore pressure was high, the elastic moduli became stable while the UCS values continued to decrease for the wet samples with the increase of water saturation level.

When rocks are saturated, the pore filling and cementing minerals are the first to absorb water and be softened, resulting in the rigid particles being surrounded by weak minerals [6]. As a result, intergranular cracks dominate when large amounts of matrix are present in the wet samples, and intragranular cracks are common in the failure of dry samples [9]. Normally, intragranular cracking releases more energy than intergranular cracking, which is why the failure of dry samples is more violent and much higher AE counts are detected. For dry samples, there is little strength difference between the frame grains and the cementations, and the micro-cracks open in the lateral direction when loaded uniaxially. In addition, the crack nucleation probably takes the shortest path and propagates along a vertical or sub-vertical direction, whether they are intra-granular or inter-granular cracks. Since an abundant amount of energy is accumulated during compression of the dry siltstone samples, multiple fractures can easily be formed along several defect areas when the sample fails. However, for the wet samples, instead of creating intragranular cracks, the cracks are more likely to propagate along the inter-granular boundaries as the cementation between grains is softened. The cracks are prone to propagate along the boundaries with the least resistance. As the grain boundaries are not

aligned, inclined shear fracture occurs. Since shear fractures can cause stress concentration at their tips, shear fractures prefer to propagate along the fracture axial direction. Based on the above analysis, transformation from multiple fracturing to single shear failure with the increase of water saturation can be expected for siltstone.

5. Conclusions

A series of uniaxial compression strength tests was conducted on low-permeability siltstone under different water saturation levels, and the water degradation effects on the mechanical properties were obvious. Based on the analysis, the following conclusions can be drawn:

(1) A negative exponential relationship is seen between the UCS and the water saturation level. The Young's modulus and thresholds for crack closure, crack initiation and crack damage all decrease significantly, even with only 10% water saturation, while an evident increase is found for the Poisson's ratio. In fact, the largest degradation for the mechanical properties between different water saturation levels (dry, 10%, 30%, 60%, 100%) are all seen between the dry and the 10% water saturation level. Therefore, precise description of the moisture content under which the tests are conducted is necessary. The volumetric strain and crack volumetric strain both decrease with the water saturation level, as the water inside the sample resists the closure of pores and fractures and makes crack initiation and propagation easier.

(2) The thresholds for crack initiation and damage are derived from the stress-strain curves and the AE performance, respectively. The thresholds obtained from AE are always a little lower than those from the stress-strain curves, as the actual deformation is later than the AE. The normalized thresholds for crack initiation and damage also decrease with the water saturation level. The average normalized ratios for the crack initiation and damage thresholds are around 31.5% and 83% respectively.

(3) By dividing the axial and lateral stress-strain curves into five equal stress zones, the stress-strain relations at different compression stages can be better described. The Young's modulus at stress zone 2 is a little higher than the tangent Young's modulus or that at stress zone 3. Since the initiated cracks are non-negligible at stress zone 3 or at half of the peak stress, the elastic moduli at stress zone 2 better represent the elastic range.

(4) Due to the low pore diameter and permeability of the siltstone samples, the induced pore pressure can affect the mechanical behaviour of wet samples, especially for those at 100% water saturation level.

(5) The softening of the cementing and clay minerals causes intergranular cracks to dominate the failure of wet samples, while for dry samples, intragranular cracks are common. A transformation from multiple fracturing to single shear failure is seen with the increase of water saturation level, accompanied by the reduction of AE activities.

Acknowledgments: Decheng Zhang would like to acknowledge the financial assistance given by China Scholarship Council towards the cost of living and the tuition fees scholarship given by the Monash University, Australia. The authors are very thankful for the help from Renji Pan and Xiya Fang at the Monash Centre for Electron Microscopy (MCEM). Also the help from Zoltan Csaki and Philip Warnes in the Civil Engineering Laboratory of Monash are appreciated.

Author Contributions: Decheng Zhang and Ranjith Pathegama Gamage designed the experiment while Decheng Zhang, Chengpeng Zhang and Wanniarachchillage Ayal Maneth Wanniarachchi conducted the experiment in the laboratory. Decheng Zhang and Ranjith Pathegama Gamage analyzed and drafted the paper. Decheng Zhang and Mandadige Samintha Anne Perera revised the paper according to the reviewers' comments.

Conflicts of Interest: The authors declare no conflict of interest.

References

1. Jeong, H.-S.; Kang, S.-S.; Obara, Y. Influence of surrounding environments and strain rates on the strength of rocks subjected to uniaxial compression. *Int. J. Rock Mech. Min. Sci.* **2007**, *44*, 321–331. [CrossRef]
2. Lashkaripour, G.R.; Ajalloeian, R. The effect of water content on the mechanical behaviour of fine-grained sedimentary rocks. In Proceedings of the ISRM International Symposium, Melbourne, Australia, 19–24 November 2000; International Society for Rock Mechanics: Salzburg, Austria, 2000.
3. Wong, L.N.Y.; Maruvanchery, V.; Liu, G. Water effects on rock strength and stiffness degradation. *Acta Geotech.* **2016**, *11*, 713–737. [CrossRef]
4. Heidari, M.; Khanlari, G.; Torabi-Kaveh, M.; Kargarian, S.; Saneie, S. Effect of porosity on rock brittleness. *Rock Mech. Rock Eng.* **2014**, *47*, 785–790. [CrossRef]
5. Yagiz, S.; Rostami, J. Indentation test for the measurement of rock brittleness. In Proceedings of the 46th U.S. Rock Mechanics/Geomechanics Symposium, Chicago, IL, USA, 24–27 June 2012; American Rock Mechanics Association: Alexandria, VA, USA, 2012.
6. Hawkins, A.; McConnell, B. Sensitivity of sandstone strength and deformability to changes in moisture content. *Q. J. Eng. Geol. Hydrogeol.* **1992**, *25*, 115–130. [CrossRef]
7. Erguler, Z.; Ulusay, R. Water-induced variations in mechanical properties of clay-bearing rocks. *Int. J. Rock Mech. Min. Sci.* **2009**, *46*, 355–370. [CrossRef]
8. Perera, M.; Ranjith, P.; Peter, M. Effects of saturation medium and pressure on strength parameters of Latrobe Valley brown coal: Carbon dioxide, water and nitrogen saturations. *Energy* **2011**, *36*, 6941–6947. [CrossRef]
9. Lin, M.-L.; Jeng, F.; Tsai, L.; Huang, T. Wetting weakening of tertiary sandstones—Microscopic mechanism. *Environ. Geol.* **2005**, *48*, 265–275. [CrossRef]
10. Josh, M.; Esteban, L.; Piane, C.D.; Sarout, J.; Dewhurst, D.; Clennell, M. Laboratory characterisation of shale properties. *J. Pet. Sci. Eng.* **2012**, *88*, 107–124. [CrossRef]
11. Hadizadeh, J.; Law, R. Water-weakening of sandstone and quartzite deformed at various stress and strain rates. *Int. J. Rock Mech. Min. Sci. Geomech. Abstr.* **1991**, *28*, 431–439. [CrossRef]
12. Duda, M.; Renner, J. The weakening effect of water on the brittle failure strength of sandstone. *Geophys. J. Int.* **2013**, *192*, 1091–1108. [CrossRef]
13. Yang, Y.; Sone, H.; Hows, A.; Zoback, M.D. Comparison of brittleness indices in organic-rich shale formations. In Proceedings of the 47th US Rock Mechanics/Geomechanics Symposium, San Francisco, CA, USA, 23–26 June 2013; American Rock Mechanics Association: Alexandria, VA, USA, 2013.
14. American Society for Testing and Materials. American Society for Testing and Materials. Standard test method for compressive strength and elastic moduli of intact rock core specimens under varying states of stress and temperatures. In *Annual Book of ASTM Standards*; American Society for Testing and Materials: West Conshohocken, PA, USA, 2004; Volume 4.
15. Eberhardt, E.; Stead, D.; Stimpson, B.; Read, R. Identifying crack initiation and propagation thresholds in brittle rock. *Can. Geotech. J.* **1998**, *35*, 222–233. [CrossRef]
16. Vásárhelyi, B. Some observations regarding the strength and deformability of sandstones in dry and saturated conditions. *Bull. Eng. Geol. Environ.* **2003**, *62*, 245–249. [CrossRef]
17. Amann, F.; Button, E.A.; Evans, K.F.; Gischig, V.S.; Blümel, M. Experimental study of the brittle behavior of clay shale in rapid unconfined compression. *Rock Mech. Rock Eng.* **2011**, *44*, 415–430. [CrossRef]
18. Yang, S.-Q.; Ranjith, P.; Huang, Y.-H.; Yin, P.-F.; Jing, H.-W.; Gui, Y.-L.; Yu, Q.-L. Experimental investigation on mechanical damage characteristics of sandstone under triaxial cyclic loading. *Geophys. J. Int.* **2015**, *201*, 662–682. [CrossRef]
19. Hickman, R.; Gutierrez, M.; de Gennaro, V.; Delage, P. A model for pore-fluid-sensitive rock behavior using a weathering state parameter. *Int. J. Numer. Anal. Methods Geomech.* **2008**, *32*, 1927–1953. [CrossRef]
20. Dyke, C.; Dobereiner, L. Evaluating the strength and deformability of sandstones. *Q. J. Eng. Geol. Hydrogeol.* **1991**, *24*, 123–134. [CrossRef]
21. Ranjith, P.; Jasinge, D.; Song, J.; Choi, S.-K. A study of the effect of displacement rate and moisture content on the mechanical properties of concrete: Use of acoustic emission. *Mech. Mater.* **2008**, *40*, 453–469. [CrossRef]
22. Zang, A.; Wagner, C.F.; Dresen, G. Acoustic emission, microstructure, and damage model of dry and wet sandstone stressed to failure. *J. Geophys. Res. Solid Earth* **1996**, *101*, 17507–17521. [CrossRef]

23. Morrow, C.; Moore, D.E.; Lockner, D. The effect of mineral bond strength and adsorbed water on fault gouge frictional strength. *Geophys. Res. Lett.* **2000**, *27*, 815–818. [CrossRef]
24. McGowen, J.M.; Gilbert, J.V.; Samari, E. Hydraulic Fracturing Down Under. In Proceedings of the SPE Hydraulic Fracturing Technology Conference, College Station, TX, USA, 29–31 January 2007; Society of Petroleum Engineers: Richardson, TX, USA, 2007.
25. Priest, S.; Selvakumar, S. *The Failure Characteristics of seLected British Rocks*; Transport and Road Research Laboratory: London, UK, 1982.
26. Wasantha, P.; Ranjith, P.; Zhao, J.; Shao, S.; Permata, G. Strain rate effect on the mechanical behaviour of sandstones with different grain sizes. *Rock Mech. Rock Eng.* **2015**, *48*, 1883–1895. [CrossRef]
27. Lajtai, E.; Schmidtke, R.; Bielus, L. The effect of water on the time-dependent deformation and fracture of a granite. *Int. J. Rock Mech. Min. Sci. Geomech. Abstr.* **1987**, *24*, 247–255. [CrossRef]
28. Verstrynge, E.; Adriaens, R.; Elsen, J.; van Balen, K. Multi-scale analysis on the influence of moisture on the mechanical behavior of ferruginous sandstone. *Constr. Build. Mater.* **2014**, *54*, 78–90. [CrossRef]
29. Szwedzicki, T. A hypothesis on modes of failure of rock samples tested in uniaxial compression. *Rock Mech. Rock Eng.* **2007**, *40*, 97–104. [CrossRef]
30. Brignoli, M.; Santarelli, F.; Papamichos, E. Capillary effects in sedimentary rocks: Application to reservoir water-flooding. In Proceedings of the 35th US Symposium on Rock Mechanics (USRMS), Reno, NV, USA, 5–7 June 1995; American Rock Mechanics Association: Alexandria, VA, USA, 1995; pp. 619–625.
31. Dieterich, J.H.; Conrad, G. Effect of humidity on time- and velocity-dependent friction in rocks. *J. Geophys. Res. Solid Earth* **1984**, *89*, 4196–4202. [CrossRef]
32. Ojo, O.; Brook, N. The effect of moisture on some mechanical properties of rock. *Min. Sci. Technol.* **1990**, *10*, 145–156. [CrossRef]